

Ages and structural and dynamical parameters of two globular clusters in the M81 group

Jun Ma,^{1,2*} Song Wang,^{1†} Zhenyu Wu,^{1,2} TianMeng Zhang,^{1,2} Hu Zou,¹ Zhimin Zhou,¹ Jundan Nie,¹ Xu Zhou,¹ Xiyang Peng,¹ Jiali Wang,¹ Jianghua Wu,³ Cuihua Du⁴ and Qirong Yuan⁵

¹Key Laboratory of Optical Astronomy, National Astronomical Observatories, Chinese Academy of Sciences, Beijing 100012, China

²College of Astronomy and Space Sciences, University of Chinese Academy of Sciences, Beijing 100049, China

³Department of Astronomy, Beijing Normal University, Beijing 100875, China

⁴School of Physics Sciences, University of the Chinese Academy of Sciences, Beijing 100049, China

⁵Department of Physics, Nanjing Normal University, WenYuan Road 1, Nanjing 210046, China

Received; Accepted

ABSTRACT

GC-1 and GC-2 are two globular clusters (GCs) in the remote halo of M81 and M82 in the M81 group discovered by Jang et al. using the *Hubble Space Telescope* (*HST*) images. These two GCs were observed as part of the Beijing–Arizona–Taiwan–Connecticut (BATC) Multicolor Sky Survey, using 14 intermediate-band filters covering a wavelength range of 4000–10000 Å. We accurately determine these two clusters’ ages and masses by comparing their spectral energy distributions (from 2267 to 20000 Å, comprising photometric data in the near-ultraviolet of the *Galaxy Evolution Explorer*, 14 BATC intermediate-band, and Two Micron All Sky Survey near-infrared *JHK_s* filters) with theoretical stellar population-synthesis models, resulting in ages of 15.50 ± 3.20 for GC-1 and 15.10 ± 2.70 Gyr for GC-2. The masses of GC-1 and GC-2 obtained here are $1.77 - 2.04 \times 10^6$ and $5.20 - 7.11 \times 10^6 M_{\odot}$, respectively. In addition, the deep observations with the Advanced Camera for Surveys and Wide Field Camera 3 on the *HST* are used to provide the surface brightness profiles of GC-1 and GC-2. The structural and dynamical parameters are derived from fitting the profiles to three different models; in particular, the internal velocity dispersions of GC-1 and GC-2 are derived, which can be compared with ones obtained based on spectral observations in the future. For the first time, in this paper, the r_h versus M_V diagram shows that GC-2 is an ultra-compact dwarf in the M81 group.

Key words: galaxies: evolution – galaxies: star clusters: general – galaxies: star clusters: individual: M81 – galaxies: star clusters: individual: M82.

1 INTRODUCTION

The study of globular clusters (GCs) plays an important role in our understanding of the evolution and history of galaxies. The Galactic GCs, the stars of which are thought to be among the oldest objects in the universe, can provide important information regarding the minimum age of the universe and the early formation history of our Galaxy. In addition, studying the spatial structures and dynamics of GCs is of great importance for understanding both their formation conditions and dynamical evolution within the tidal fields of their galaxies (Barmby et al. 2007).

The most direct method to determine a cluster’s age is by em-

ploying main-sequence photometry, since the absolute magnitude of the main-sequence turn-off is predominantly affected by age (see Puzia et al. 2002, and references therein). However, this method was mainly applied to the star clusters in the Milky Way and its satellites (e.g. Rich, Shara & Zurek 2001). Generally, the ages of extragalactic star clusters are determined by comparing their observed spectral energy distributions (SEDs) and/or spectroscopy with the predictions of simple stellar population (SSP) models (see Ma et al. 2010, and references therein).

The structural and dynamical parameters of clusters are often determined by fitting the surface brightness profiles to a number of different models, combined with mass-to-light ratios (M/L values) estimated from velocity dispersions or population-synthesis models. We only mention three models that will be used in this paper. The first is based on a single-mass, isotropic, modified isothermal

* E-mail: majun@nao.cas.cn

† E-mail: somgw@bao.ac.cn

sphere developed by King (1966). The second is a further modification of a single-mass, isotropic isothermal sphere based on the ad hoc stellar distribution function of Wilson (1975). The third model is based on the $R^{1/n}$ surface density profile of Sérsic (1968). Using the three models, some authors have achieved some success in determining structural and dynamical parameters of clusters in the Local galaxies: the Milky Way, the Large and Small Magellanic Clouds, Fornax and Sagittarius dwarf spheroidal galaxies (McLaughlin & van der Marel 2005), M31 (Barmby et al. 2007, 2009; Wang & Ma 2013), NGC 5128 (McLaughlin et al. 2008), and M33 (Ma 2015).

Except for the Local Group galaxies, the M81 group includes the nearest large spirals outside the Local Group. M81 locates in the centre of the M81 group, and 36 member galaxies surround M81 (Chiboucas et al. 2013). Although the GC system of M81 has come under recent detailed scrutiny (see Ma et al. 2013, and references therein), however structural and dynamical studies of the GC system of the M81 group are very limited: Chandar, Ford & Tsvetanov (2001) estimated the core radii of 114 compact star clusters of M81 based on the *Hubble Space Telescope* (*HST*)/Wide Field and Planetary Camera 2 imaging; Nantais et al. (2011) estimated the effective radii of 419 GC candidates of M81 using *HST*/Advanced Camera for Surveys (ACS) imaging; and Lim, Hwang & Lee (2013) estimated the effective radii of 1105 star clusters in M82 using *HST*/ACS imaging. Jang et al. (2012) and Mayya et al. (2013) determined structural parameters for three GCs in the M81 group by fitting the King models to the surface brightness profiles of the *HST* images. However, for two of them (i.e. GC-1 and GC-2), Jang et al. (2012) only derived their core and half-light radii. GC-1 and GC-2 are of interest because they are in the remote haloes of M81 and M82 in the M81 group recently discovered by Jang et al. (2012); in particular, GC-2 is the most isolated GC in the local universe. So, we will derive the structural and dynamical parameters of GC-1 and GC-2. In addition, we will also accurately determine these two clusters' ages and masses by comparing their SEDs with theoretical stellar population-synthesis models.

The distances were taken to be $(m - M)_0 = 27.80 \pm 0.03$ to GC-1 and $(m - M)_0 = 28.04 \pm 0.04$ to GC-2 throughout, which were derived by Jang et al. (2012).

In this paper, we will determine the ages and masses, and structural and dynamical parameters, for GC-1 and GC-2. We will describe the details of the observations and our approach to the data reduction with the Beijing–Arizona–Taiwan–Connecticut (BATC) system in Section 2 and with the *HST* programs in Sections 2 and 4. We will determine the ages and masses of GC-1 and GC-2 by comparing observational SEDs with population-synthesis models in Section 3, and determine structural and dynamical parameters of GC-1 and GC-2 in Section 5. We make comparison to previous results and discussion in Section 6, and provide a summary in Section 7.

2 ARCHIVAL IMAGES OF BATC, 2MASS, GALEX AND *HST*

In this section, we will determine the magnitudes of GC-1 and GC-2 based on the archival images of the BATC Multicolor Sky Survey, Two Micron All Sky Survey (2MASS) and *Galaxy Evolution Explorer* (*GALEX*) using a standard aperture photometry approach, i.e. the PHOT routine in DAOPHOT (Stetson 1987). In addition, we will also describe *HST* observations as well as magnitude transformation in this section.

2.1 Intermediate-band photometry

The M81 field is part of a galaxy calibration program of the BATC Multicolor Sky Survey. The BATC program uses the 60/90 cm Schmidt Telescope at the Xinglong Station of the National Astronomical Observatories, Chinese Academy of Sciences. This system includes 15 intermediate-band filters, covering a range of wavelength from 3000 to 10000 Å (see Fan et al. 1996, for details). In order to study the stellar populations of GC-1 and GC-2, we extracted 322 images of M81 field as part of the BATC Multicolor Sky Survey, taken in 14 intermediate-band filters with a total exposure time of ~ 100 h from February 5, 1995 to April 30, 2002. These images were observed in the good nights including the photometric nights. The images of one filter were observed as possible as in the same night. The dome flat-field images were taken by using an isotropic diffuser right in front of the Schmidt corrector plate (the entrance pupil of the telescope) (see Zhou et al. 2004, for details). The images were reduced with standard procedures, including bias subtraction and flat-fielding of the CCD images, with an automatic data reduction software named PIPELINE 1, developed for the BATC Multicolor Sky Survey (Fan et al. 1996; Zheng et al. 1999). Also in PIPELINE 1, the astrometric plate solution is obtained by registering the brighter stars in each image with the *HST* Guide Star Catalogue (GSC) coordinate system (Jenkner et al. 1990). The positions of the stars in the images (x and y) then can be easily transformed to the equatorial coordinates (α and β) in J2000. The final RMS errors in positional accuracy of the stars are about 0.5 arcsec. Then, the multiple images of the same filter were combined to improve the signal-to-noise ratios (SNRs), and the cosmic rays and bad pixels were corrected by comparison of multiple images during combination. Before the combination, the other images were shifted and rotated according to one image. The images observed in different exposures were then stacked in the combination.

Calibration of the magnitude zero level in the BATC photometric system is similar to that of the spectrophotometric AB magnitude system. For flux calibration, the Oke-Gunn (Oke & Gunn 1983) primary flux standard stars HD 19445, HD 84937, BD +26°2606 and BD +17°4708 were observed during photometric nights (Yan et al. 2000). On the photometric nights, two or more standard stars as well as the BATC programmed fields were observed between air masses of 1 and 2. The standard stars are observed as frequently as possible using the central part of the CCD (size 300×300) for saving readout time and disc space. The extinction coefficient and magnitude zero obtained from the standard stars are used for making the flux calibration on the BATC programmed field images. The exposure times of the BATC programmed fields are 300 s (i.e. in short exposures). Using the images of the standard stars observed on the photometric nights, the extinction coefficients at any given time in a night and the zero point of the instrumental magnitude are obtained. The instrumental magnitudes M_{inst} of selected bright, isolated stars in the BATC programmed field images observed in short exposures can be readily transformed to the BATC AB magnitude system M_{batc} , and then these bright, isolated stars were taken as secondary standards and were subsequently used to perform calibration on the combined image. Table 1 lists the parameters of the BATC Multicolor Filter System and the statistics of observations. Column 7 of Table 1 gives the errors of flux calibration in each filter.

Fig. 1 shows the finding charts of GC-1 and GC-2 in the BATC g band.

To determine the total luminosities of GC-1 and GC-2, we produced curves of growth from the g -band photometry obtained

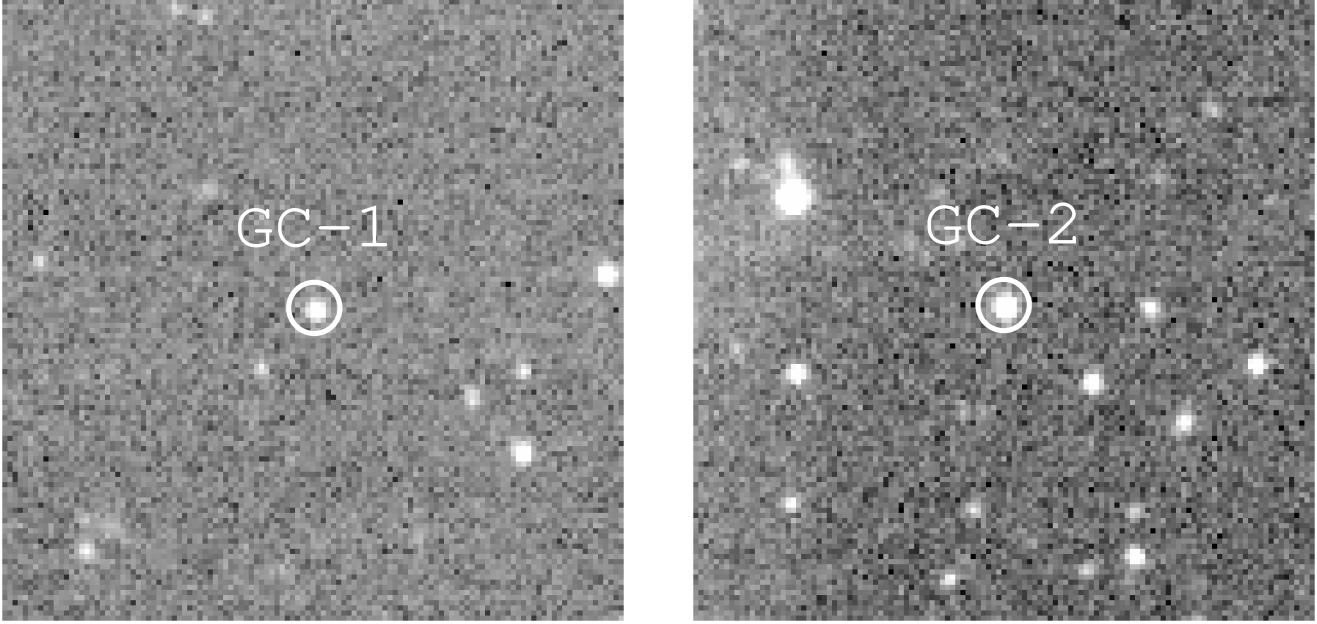


Figure 1. Images of GC-1 and GC-2 in the BATC g band obtained with the 60/90 cm Schmidt telescope. The circles are photometric apertures used in this paper.

Table 1. Parameters of the BATC filters and statistics of observations for M81 field.

No.	Name	cw (\AA) ^a	FWHM (\AA) ^b	Exp. (h) ^c	N.img ^d	rms ^f
1	<i>b</i>	3890	291	03:40	11	0.009
2	<i>c</i>	4210	309	03:53	14	0.004
3	<i>d</i>	4546	332	12:20	39	0.013
4	<i>e</i>	4872	374	06:10	21	0.005
5	<i>f</i>	5250	344	06:05	19	0.005
6	<i>g</i>	5785	298	05:12	18	0.004
7	<i>h</i>	6075	308	04:00	12	0.006
8	<i>i</i>	6710	491	06:00	18	0.006
9	<i>j</i>	7010	238	05:20	16	0.007
10	<i>k</i>	7530	192	05:40	17	0.013
11	<i>m</i>	8000	255	05:20	16	0.006
12	<i>n</i>	8510	167	15:00	45	0.005
13	<i>o</i>	9170	247	16:40	50	0.036
14	<i>p</i>	9720	275	08:40	26	0.039

^a Central wavelength for each BATC filter.

^b Passband width for each BATC filter.

^c A total exposure time for each BATC filter.

^d Image numbers for each BATC filter.

^f Calibration error, in magnitude, for each filter as obtained from the standard stars.

through apertures with radii in the range 2–11 pixel with 1 pixel increments. These curves of growth were used to determine the aperture size required to enclose the total cluster light. The most appropriate photometric radius that includes all light from the objects is adopted independently for each cluster. The local sky background was measured in an annulus with an inner radius which being larger 1 pixel than photometric radius and ~ 8.4 arcsec wide, in which the mode was used. Finally, we obtained photometry for GC-1 and GC-2 in the individual 14 intermediate-band filters. Table 2 lists our new magnitudes, with errors given by IRAF/DAOPHOT.

Column (1) gives the cluster names. The 1σ magnitude uncertainties from DAOPHOT are listed for each object on the second line for the corresponding bands. Sources of CCD photometric error of the BATC photometric system include: photon statistics; read-out noise; random and systematic errors from bias subtraction and flat-fielding, and image defects, and possible non-linearity of the CCD. The analysis program DAOPHOT gives the theoretical prediction of the error based on the photon statistics it measures, which is included in Table 2. Fan et al. (1996) have analyze the other errors in detail, and found that these errors are not larger than 0.02 mag for stars brighter than $m = 16$ in most filters.

2.2 Near-infrared 2MASS photometry

We used the 2MASS archival images of GC-1 and GC-2 in the JHK_s bands to do photometry. The images were retrieved using the 2MASS Batch Image Service¹. The uncompressed atlas images were used with a resampled spatial resolution of ~ 1 arcsec pixel⁻¹. The photometry routine we used is also IRAF/DAOPHOT (Stetson 1987).

We determine the total luminosity of each object in the JHK_s bands based on the processes in Section 2.1. We produced a curve of growth from the J -band photometry obtained through apertures with radii in the range of 3–14 pixel with 1 pixel increments. The local sky background was measured in an annulus with an inner radius 1 pixel larger than the photometric radius and 5 pixels wide. At last, the instrumental magnitudes were then calibrated using the relevant zero points obtained from the photometric header keywords of each image. The calibrated photometry of GC-1 and GC-2 in J , H and K_s bands is summarized in Table 2, in conjunction with the 1σ magnitude uncertainties obtained from DAOPHOT. The photometry of GC-1 in K_s cannot be obtained here because of low SNRs. In

¹ <http://irsa.ipac.caltech.edu/applications/2MASS/IM/batch.html>.

Table 2. BATC, 2MASS and GALEX photometry of GC-1 and GC-2 in the M81 group.

ID	<i>b</i> (mag)	<i>c</i> (mag)	<i>d</i> (mag)	<i>e</i> (mag)	<i>f</i> (mag)	<i>g</i> (mag)	<i>h</i> (mag)	<i>i</i> (mag)	<i>j</i> (mag)	<i>k</i> (mag)	<i>m</i> (mag)	<i>n</i> (mag)	<i>o</i> (mag)	<i>p</i> (mag)	<i>J</i> (mag)	<i>H</i> (mag)	<i>K_s</i> (mag)	NUV (mag)
GC-1	19.715	19.326	19.221	18.989	18.835	18.539	18.454	18.328	18.278	18.106	17.997	18.012	17.915	17.857	17.060	16.449	...	22.974
	0.270	0.224	0.039	0.024	0.019	0.035	0.028	0.009	0.030	0.030	0.033	0.038	0.072	0.104	0.029	0.021	...	0.427
GC-2	18.934	19.057	18.260	18.077	17.868	17.617	17.486	17.401	17.315	17.208	17.112	17.108	16.901	16.856	15.897	15.587	15.207	22.134
	0.106	0.112	0.017	0.011	0.010	0.016	0.011	0.005	0.014	0.015	0.015	0.013	0.028	0.051	0.017	0.014	0.012	0.290

addition, since the observed magnitudes in the 2MASS photometric system are given in the Vega system, we transformed them to the AB system for our fits (see Section 3.3 for details). The photometric offsets in the 2MASS filters between the Vega and AB systems were obtained on the basis of equations (7) and (8) in the manual provided by Bruzual & Charlot (2003, hereafter BC03).

2.3 GALEX ultraviolet photometry

We used the *GALEX* archival images of GC-1 and GC-2 in the FUV and NUV bands to do photometry. The images were retrieved using the *GALEX* Batch Image Service². The exposure times were 14706.7 s in the FUV band and 29421.55 s in the NUV band, respectively. The images were sampled with 1.5'' pixels. The relevant zero-points for photometry are 20.08 and 18.82 in the NUV and FUV magnitudes, respectively (Morrissey et al. 2007).

We determine the total luminosity of each object in the FUV and NUV bands using the processes in Section 2.1. We produced a curve of growth from the NUV-band photometry obtained through apertures with radii in the range of 2–13 pixel with 1 pixel increments. The calibrated photometry of GC-1 and GC-2 in the NUV band is summarized in Table 2. The photometry of GC-1 and GC-2 in the FUV band cannot be obtained here because of low SNRs. It is known that the *GALEX* photometric system is calibrated to match the spectrophotometric AB system (Rey et al. 2007) as the BATC photometric system does.

2.4 HST observation

The observations used here come from the *HST* program 11613 (P.I.: de Jong), in which GC-1 was observed by the *HST*/ACS/WFC in the *F606W* and *F814W* bands, and GC-2 was observed by the *HST*/Wide Field Camera 3 (WFC3)/UVIS in the *F606W* and *F814W* bands. GC-1 was observed with a total exposure time of 850 s in the *F606W* band and 690 s in the *F814W* band, and GC-2 was observed with a total exposure time of 735 s in the *F606W* band and 1225 s in the *F814W* band. We obtained the combined drizzled images from the Hubble Legacy Archive. In addition, for easy comparison with catalogues of the GCs in the Milky Way in the future work, we transform the ACS/WFC and WFC3/UVIS magnitudes in the *F606W* band to the standard *V*. Wang & Ma (2012) has presented transformation from ACS/WFC magnitude to standard *V* magnitude in their equation (7). However, till now transformations from WFC3/UVIS to standard *V* magnitude has not been presented in any references. We used equation (7) of Wang & Ma (2012) for the transformation in this paper, and *V* and *I* magnitudes are obtained in this paper (see Section 3.4 in detail). We rewrite equation (7) of Wang & Ma (2012) below:

$$(V - F606W)_0 = -0.067 + 0.340(V - I)_0 - 0.038(V - I)_0^2. \quad (1)$$

² <http://galex.stsci.edu/GR6/>.

We will use these *HST* images to derive the structural and dynamical parameters of GC-1 and GC-2 (see Sections 4 and 5 for details).

3 STELLAR POPULATION

3.1 Metallicities and reddening values

Cluster SEDs are determined by the combination of their ages and metallicities, which is often referred to as the age–metallicity degeneracy. Therefore, the age of a cluster can only be constrained accurately if the metallicity is determined independently with confidence. For GC-1 and GC-2, only Jang et al. (2012) determined their metallicities. These authors presented the color–magnitude diagrams for GC-1 and GC-2, and derived the metallicities to be $[\text{Fe}/\text{H}] = -2.23 \pm 0.11$ for GC-1 and $[\text{Fe}/\text{H}] = -2.23 \pm 0.12$ for GC-2 based on the mean colour of the red giant branch stars. In addition, Jang et al. (2012) derived the metallicity of GC-2 to be $[\text{Fe}/\text{H}] = -2.3 \pm 0.12$ based on its optical spectrum observed by the Sloan Digital Sky Survey (SDSS). Here we adopted the values of metallicity from Jang et al. (2012): $[\text{Fe}/\text{H}] = -2.23 \pm 0.11$ for GC-1 and $[\text{Fe}/\text{H}] = -2.3 \pm 0.12$ for GC-2.

In order to obtain intrinsic SEDs of GC-1 and GC-2, the photometry must be corrected for reddening. Since GC-1 and GC-2 are in the remote haloes of M81 and M82, only the foreground extinction contribution of the Milky Way is considered. The dust map of Schlegel, Finkbeiner & Davis (1998) presents $E(B - V) = 0.09$ for GC-1 and $E(B - V) = 0.10$ for GC-2 (see also Jang et al. 2012 and Monachesi et al. 2013).

3.2 Stellar populations and synthetic photometry

To determine the ages and masses of GC-1 and GC-2, we compared their SEDs with theoretical stellar population–synthesis models. The SEDs consist of photometric data in the NUV band of *GALEX*, 14 BATC intermediate-band and 2MASS near-infrared (NIR) *JHK_s* filters obtained in this paper. GC-1 and GC-2 are both very metal poor (see Section 3.1). So, we use the SSP models of BC03, which provide the evolution of the spectra and photometric properties for a wide range of stellar metallicities. For example, BC03 SSP models based on the Padova-1994 evolutionary tracks include six initial metallicities: $Z = 0.0001, 0.0004, 0.004, 0.008, 0.02 (Z_{\odot}),$ and 0.05 , corresponding to $[\text{Fe}/\text{H}] = -2.25, -1.65, -0.64, -0.33, +0.09,$ and $+0.56$. In this paper, we adopt the high-resolution SSP models using the Padova-1994 evolutionary tracks to determine the most appropriate ages for GC-1 and GC-2. And a Salpeter (1955) initial mass function (IMF) is also used. These SSP models contain 221 spectra describing the spectral evolution of SSPs from 1.0×10^5 yr to 20 Gyr. The evolving spectra include the contribution of the stellar component at wavelengths from 91 Å to 160 μm.

Since our observational data are integrated luminosities

through a given set of filters, we convolved the theoretical SSP SEDs of BC03 with the *GALEX* NUV, BATC $b - p$ and 2MASS JHK_s filter response curves to obtain synthetic optical and NIR photometry for comparison. The synthetic i th filter magnitude can be computed by

$$m = -2.5 \log \frac{\int_{\lambda} F_{\lambda} \varphi_i(\lambda) d\lambda}{\int_{\lambda} \varphi_i(\lambda) d\lambda} - 48.60, \quad (2)$$

where F_{λ} is the theoretical SED, and φ_i is the response function of the i th filter of the *GALEX*, BATC and 2MASS photometric systems. Here, F_{λ} varies with age and metallicity.

3.3 Fit Results

We use a χ^2 minimization approach to examine which SSP models are most compatible with the observed SEDs of GC-1 and GC-2, following

$$\chi^2 = \sum_{i=1}^N \frac{[m_{\lambda_i}^{\text{intr}} - m_{\lambda_i}^{\text{mod}}(t)]^2}{\sigma_i^2}, \quad (3)$$

where $m_{\lambda_i}^{\text{mod}}(t)$ is the integrated magnitude in the i th filter of a theoretical SSP at age t , $m_{\lambda_i}^{\text{intr}}$ represents the intrinsic integrated magnitude in the same filter, and

$$\sigma_i^2 = \sigma_{\text{obs},i}^2 + \sigma_{\text{mod},i}^2 + \sigma_{\text{md},i}^2. \quad (4)$$

Here, $\sigma_{\text{obs},i}$ is the observational uncertainty from Table 2 of this paper, $\sigma_{\text{mod},i}$ is the uncertainty associated with the model itself, and $\sigma_{\text{md},i}$ is associated with the uncertainty with the distance modulus adopted here. Following Ma et al. (2012), we adopt $\sigma_{\text{mod},i} = 0.05$ mag. For $\sigma_{\text{md},i}$, we adopt 0.03 and 0.04 for GC-1 and GC-2, respectively, which are from Jang et al. (2012). N is the number of photometries used in the fitting.

Before fitting, we obtained the theoretical SEDs for the metallicity $[\text{Fe}/\text{H}] = -2.23$ model by interpolation of between $[\text{Fe}/\text{H}] = -2.25$ and -1.65 models for GC-1. For GC-2, we used the theoretical SEDs for the metallicity $[\text{Fe}/\text{H}] = -2.25$ model for fitting.

For every fit we obtain a value for the reduced χ^2 , and $\chi^2_{\nu} = \chi^2/\nu$, where ν is the number of free parameters, i.e. the number of observational data points minus the number of parameters used in the theoretical model. For a good fit, χ^2_{ν} should be about unity. The fit with the minimum value of χ^2_{ν} [hereafter $\chi^2_{\nu}(\text{min})$] was adopted as the best fit and age was adopted. This method was applied for fits with the BC03 models. To estimate the uncertainty in the determined age we use confidence limits. If $\chi^2_{\nu} < \chi^2_{\nu}(\text{min}) + 1$ then the resulting age is within the 68.3 per cent probability range. So the accepted range in age is derived from the fits which have $\chi^2_{\nu}(\text{min}) < \chi^2_{\nu} < \chi^2_{\nu}(\text{min}) + 1$. With this method we derived the ages with their uncertainties of GC-1 and GC-2. For GC-1, the best-reduced $\chi^2_{\nu}(\text{min}) = 0.7$ is achieved with an age of 15.50 ± 3.20 Gyr when the value of $E(B - V)$ is adopted to be 0.09, and $\nu = 16$. For GC-2, the best-reduced $\chi^2_{\nu}(\text{min}) = 2.9$ is achieved with an age of 15.10 ± 2.70 Gyr when the value of $E(B - V)$ is adopted to be 0.10, and $\nu = 16$. The values for the extinction coefficient, R_{λ} , are obtained by interpolating the interstellar extinction curve of Cardelli, Clayton & Mathis (1989). Fig. 2 shows the intrinsic SEDs of GC-1 and GC-2, the integrated SEDs of the best-fitting models and the spectra of the best-fitting models. From Fig. 2, we can see that, for GC-2, the BC03 SSP models cannot fit the photometric datum in the c band as well as the other 17 photometric data, i.e. the observed magnitude is dimmer than that of the model in the c band.

We have not been able to identify the cause of this discrepancy. Direct inspection of the image in the c band clearly shows that GC-2 is not unusual. Also, we used the same image to determine the photometries for GC-1 and GC-2 at the same time. So, we argued that this discrepancy may be from the intrinsic property of GC-2, i.e. it is caused by the intrinsic luminosity of stellar populations of GC-2. In the fitting, we did not use the magnitude in the c band. In addition, it is evident that the ages of GC-1 and GC-2 obtained here based on the BC03 models are greater than the currently accepted age of the universe. However, we must keep in mind that the BC03 SSP models were calculated for ages up to 20 Gyr. In fact, ages derived for objects such as GCs and galaxies in excess of that of the universe only mean that these objects are among the oldest objects in the universe.

3.4 Masses

We next determine the masses of GC-1 and GC-2. The BC03 SSP models are normalized to a total mass of $1 M_{\odot}$ in stars at age $t = 0$. The absolute magnitudes (in the Vega system) in $UBVRI$ and 2MASS JHK_s filters are included in the BC03 SSP models. The difference between the intrinsic absolute magnitudes and those given by the model provides a direct measurement of the cluster mass. To reduce mass uncertainties resulting from photometric uncertainties based on only magnitudes in one filter (in general the V band is used), we estimated the masses of GC-1 and GC-2 using magnitudes in the $UBVRI$ and JHK_s bands. Zhou et al. (2003) have derived the relationships between the BATC intermediate-band system and the broad-band system. However, we cannot derive the magnitudes in the U band since the magnitudes in the a band cannot be obtained in this paper. The magnitudes in the $BVRI$ bands are obtained using the photometries of the BATC intermediate-band system obtained here (see Table 2 for details) and the relationships between these two systems in Zhou et al. (2003). The $BVRI$ magnitudes are $B = 19.42 \pm 0.083$, $V = 18.71 \pm 0.032$, $R = 18.43 \pm 0.009$ and $I = 17.73 \pm 0.025$ for GC-1, and $B = 18.60 \pm 0.039$, $V = 17.79 \pm 0.016$, $R = 17.51 \pm 0.005$ and $I = 16.78 \pm 0.001$ for GC-2. The resulting mass determinations for GC-1 and GC-2 are listed in Table 3 with their 1σ uncertainties. Table 3 shows that the masses of GC-1 and GC-2 obtained based on the magnitudes in different bands are consistent.

4 HST DATA ANALYSIS

4.1 Ellipticity, position angle and surface brightness profile

The imaging data that we used in this work to obtain the structural and dynamical parameters of GC-1 and GC-2 come from the *HST* observations in the $F606W$ and $F814W$ bands (see Section 2.4 for details). The data analysis procedures used to measure the surface brightness profiles of clusters have been described in Barmby et al. (2007); here we briefly summarize the procedures. The surface photometries of each cluster were obtained from the drizzled images using the IRAF task ELLIPSE. The centre position of each cluster was fixed at a value derived by the object locator of the ELLIPSE task; however an initial centre position was determined by centroiding. Elliptical isophotes were fitted to the data, with no sigma clipping. We ran two passes of the ELLIPSE task: the first pass was run in the usual way, i.e. the ellipticity and position angle (PA) vary with the isophote semimajor axis. In the second pass the surface brightness profiles on fixed, zero-ellipticity isophotes were measured, since

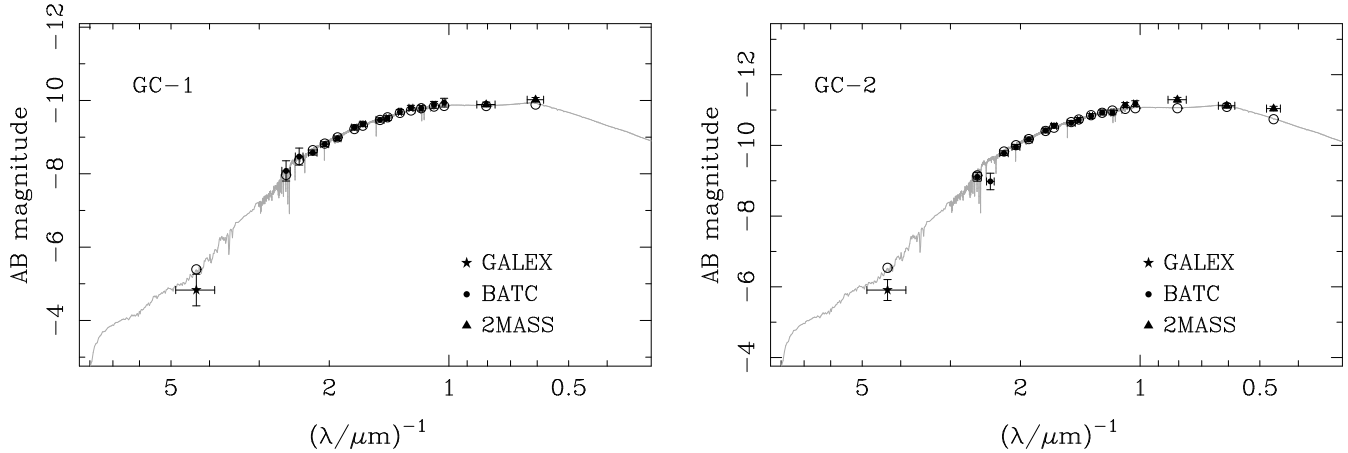


Figure 2. Best-fitting, integrated theoretical BC03 SEDs compared to the intrinsic SEDs of GC-1 and GC-2. The photometric measurements are shown as symbols with error bars (vertical error bars for photometric uncertainties and horizontal ones for the approximate wavelength coverage of each filter). The open circles represent the calculated magnitudes of the model SED for each filter.

Table 3. Mass estimates of GC-1 and GC-2 based on the BC03 models.

	<i>B</i>	<i>V</i>	<i>R</i>	<i>I</i>	<i>J</i>	<i>H</i>	<i>K_s</i>
	Mass ($10^6 M_{\odot}$)						
GC-1	1.93 ± 0.15	1.97 ± 0.06	1.77 ± 0.01	2.04 ± 0.05	1.87 ± 0.05	2.04 ± 0.04	...
GC-2	5.20 ± 0.19	5.81 ± 0.09	5.25 ± 0.02	6.08 ± 0.01	6.78 ± 0.11	5.61 ± 0.07	7.11 ± 0.08

we chose to fit circular models for the intrinsic cluster structure and the point spread function (PSF) as in Barmby et al. (2007). Fig. 3 and 4 plot the ellipticity ($\epsilon = 1 - b/a$) and PA as a function of the semimajor axis length (a) in the *F606W* and *F814W* bands for GC-1 and GC-2. The errors were generated by the IRAF task ELLIPSE, in which the ellipticity errors were obtained from the internal errors in the harmonic fit, after removal of the first and second fitted harmonics. The ellipticities and PAs measured on images in different filters track well together, as we would expect. Figs 3 and 4 show that the PAs are occasionally wildly varying. This is likely to be produced by internal errors in the ELLIPSE task. The final ellipticity and PA for each cluster were calculated as the average of the values obtained in the first pass of ELLIPSE task, which are listed in Table 4. Errors correspond to the standard deviation of the mean. From Figs 3 and 4, and Table 4, we can see that the ellipticities of GC-1 and GC-2 are less than 0.1, which are consistent with the mean value of 0.07 ± 0.01 for the Milky Way GCs (White & Shawl 1987) and the mean $\epsilon = 0.11 \pm 0.01$ for the M31 GCs (Barmby, Holland & Huchra 2002).

Raw output from package ELLIPSE is in terms of counts s^{-1} pixel $^{-1}$, which needs to multiply by a number (400 for ACS/WFC, and 625 for WFC3/UVIS) to convert to counts s^{-1} arcsec $^{-2}$. A formula is used to transform the counts to surface brightness in magnitudes calibrated on the VEGAMAG system,

$$\mu/\text{mag arcsec}^{-2} = -2.5 \log(\text{counts } s^{-1} \text{ arcsec}^{-2}) + \text{Zeropoint}. \quad (5)$$

As noted by Barmby et al. (2007), occasional oversubtraction of the background during the multidrizzling in the automatic reduction pipeline leads to “negative” counts in some pixels, so we worked in terms of linear intensity instead of surface brightness in magnitudes as Barmby et al. (2007) did. With updated absolute magnitudes of the Sun, M_{\odot} (C. Willmer, private communication)

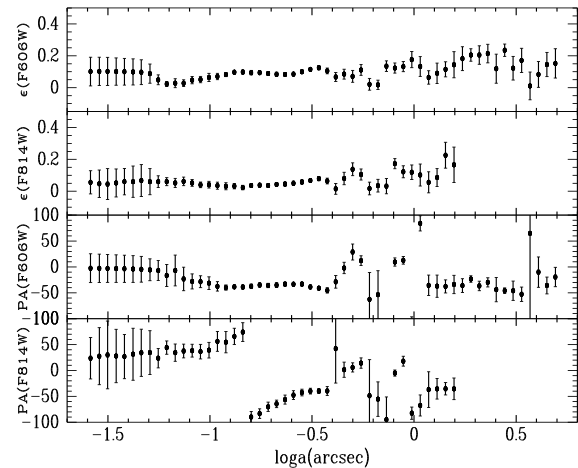


Figure 3. Ellipticity (ϵ) and PA as a function of the semimajor axis (a) in the *F606W* and *F814W* filters of *HST/ACS/WFC* for GC-1.

listed in Table 5, the equation for transforming counts to surface brightness in intensity is derived as below,

$$I/L_{\odot} \text{ pc}^{-2} \approx \text{Conversion Factor} \times (\text{counts } s^{-1} \text{ arcsec}^{-2}). \quad (6)$$

Converting from luminosity density in $L_{\odot} \text{ pc}^{-2}$ to surface brightness in magnitude was done according to

$$\mu/\text{mag arcsec}^{-2} = -2.5 \log(I/L_{\odot} \text{ pc}^{-2}) + \text{Coefficient}. \quad (7)$$

The zero-points, conversion factors and coefficients used in these transformations for each filter are also listed in Table 5. In this paper, the final, calibrated intensity profiles for GC-1 and GC-2 with no extinction correction are listed in Table 6. The reported

Table 4. Basic parameters of GC-1 and GC-2 in the M81 group.

ID	ϵ^a	θ^a (deg E of N)	ϵ^b	θ^b (deg E of N)	$E(B-V)^c$	[Fe/H] ^d	Age ^e (Gyr)
(1)	(2)	(3)	(4)	(5)	(6)	(7)	(8)
GC-1	0.10 ± 0.01	60 ± 1	0.07 ± 0.02	80 ± 5	0.09	-2.23 ± 0.11	15.50 ± 3.20
GC-2	0.08 ± 0.01	-92 ± 10	0.09 ± 0.01	-106 ± 1	0.10	-2.30 ± 0.12	15.10 ± 2.70

^a ϵ and θ are ellipticity and PA of *F606W* filter for each cluster, respectively, which were obtained in this paper.

^b ϵ and θ are ellipticity and PA of *F814W* filter for each cluster, respectively, which were obtained in this paper.

^c $E(B-V)$ is the reddening value of each cluster adopted in this paper.

^d [Fe/H] is the metallicity of each cluster adopted in this paper.

^e Age is the age of each cluster obtained in this paper.

Table 5. Calibration data for the *HST* images.

Filter	Pivot λ (Å)	R_λ^a	Zeropoint ^b	M_\odot^c	Conversion Factor ^d	Coefficient ^e
(1)	(2)	(3)	(4)	(5)	(6)	(7)
Calibration Data for ACS/WFC images						
<i>F606W</i>	5921.1	2.85	26.398	4.611	0.8207	26.183
<i>F814W</i>	8057.0	1.83	25.501	4.066	1.1349	25.638
Calibration Data for WFC3/UVIS images						
<i>F606W</i>	5887.0	2.87	25.987	4.640	1.2312	26.212
<i>F814W</i>	8024.0	1.84	24.680	4.100	2.4937	25.672

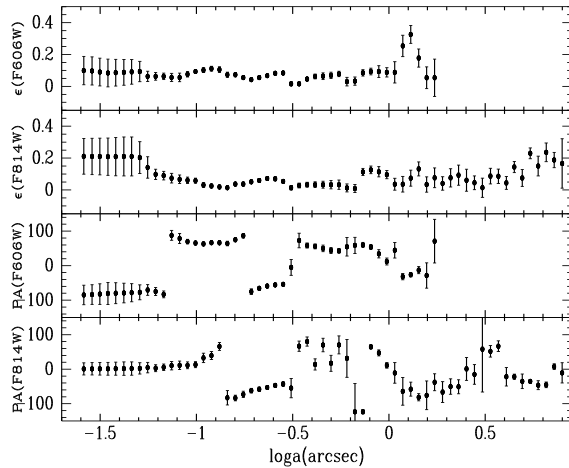
^a $A_\lambda = R_\lambda \times E(B-V)$.

^b Additive conversion between surface brightness in counts $s^{-1} \text{ arcsec}^{-2}$ and magnitude in mag arcsec^{-2} .

^c Updated absolute magnitude of the Sun (C. Willmer, private communication).

^d Multiplicative conversion between surface brightness in counts $s^{-1} \text{ arcsec}^{-2}$ and intensity in $L_\odot \text{ pc}^{-2}$.

^e Additive conversion between surface brightness in magnitude in mag arcsec^{-2} and intensity in $L_\odot \text{ pc}^{-2}$.

**Figure 4.** Ellipticity (ϵ) and PA as a function of the semimajor axis (a) in the *F606W* and *F814W* filters of *HST*/WFC3/UVIS for GC-2.

intensities are calibrated on the *VEGAMAG* scale. In Table 6, Column 7 gives a flag for each point, which has the same meaning as defined by Barmby et al. (2007) and McLaughlin et al. (2008). The points flagged with ‘OK’ are used to constrain the model fit, while the points flagged with ‘DEP’ are those that may lead to excessive weighting of the central regions of clusters (see Barmby et al. 2007; McLaughlin et al. 2008, for details). In addition, points marked with ‘BAD’ are those individual isophotes that deviated strongly from their neighbors or showed irregular features, which were deleted by hand.

Table 6. Intensity profiles for GC-1 and GC-2 in the M81 group.

ID	Detector	Filter	R^a (arcsec)	I ($L_\odot \text{ pc}^{-2}$)	Uncertainty ($L_\odot \text{ pc}^{-2}$)	Flag
(1)	(2)	(3)	(4)	(5)	(6)	(7)
GC-1	ACS/WFC	<i>F606W</i>	0.0260	8027.168	152.402	OK
	ACS/WFC	<i>F606W</i>	0.0287	7939.514	166.932	DEP
	ACS/WFC	<i>F606W</i>	0.0315	7843.411	182.646	DEP
	ACS/WFC	<i>F606W</i>	0.0347	7738.249	199.672	DEP
	ACS/WFC	<i>F606W</i>	0.0381	7623.505	218.122	DEP
	ACS/WFC	<i>F606W</i>	0.0420	7498.559	238.123	DEP
	ACS/WFC	<i>F606W</i>	0.0461	7362.532	259.738	DEP
	ACS/WFC	<i>F606W</i>	0.0508	7211.208	282.077	DEP
	ACS/WFC	<i>F606W</i>	0.0558	6985.240	292.158	OK
	ACS/WFC	<i>F606W</i>	0.0614	6723.962	300.276	DEP
	ACS/WFC	<i>F606W</i>	0.0676	6413.738	305.292	DEP
	ACS/WFC	<i>F606W</i>	0.0743	6069.431	303.803	DEP
	ACS/WFC	<i>F606W</i>	0.0818	5690.524	307.635	OK
	ACS/WFC	<i>F606W</i>	0.0899	5265.273	304.361	DEP
	ACS/WFC	<i>F606W</i>	0.0989	4809.377	306.135	DEP
	ACS/WFC	<i>F606W</i>	0.1088	4313.025	273.523	DEP
	ACS/WFC	<i>F606W</i>	0.1197	3832.797	238.625	DEP
	ACS/WFC	<i>F606W</i>	0.1317	3417.995	209.960	OK
	ACS/WFC	<i>F606W</i>	0.1448	2942.204	178.856	OK
	ACS/WFC	<i>F606W</i>	0.1593	2425.916	142.266	OK

^a R is the clustercentric radius.

Note. This table is available in its entirety in machine-readable form.

4.2 Point-spread function

The PSF models are critical to accurately measure the shapes of the objects in images taken with *HST* (Rhodes et al. 2006). In this paper, we chose not to deconvolve the data, instead fitting the structural models after convolving them with a simple analytic description of the PSF as Barmby et al. (2007) and Wang & Ma (2013) did (see Barmby et al. 2007; Wang & Ma 2013, for details) for M31 star clusters. A simple analytic description of the PSFs for the ACS/WFC filters has been given by Wang & Ma (2013). In ad-

Table 7. Coefficients for the PSF models.

Detector	Filter	r_0 (arcsec)	α	β
(1)	(2)	(3)	(4)	(5)
ACS/WFC	<i>F606W</i>	0.053	3	3.14
	<i>F814W</i>	0.056	3	3.05
WFC3/UVIS	<i>F606W</i>	0.050	3	3.24
	<i>F814W</i>	0.058	3	3.50

dition, we derived the WFC3/UVIS PSF models using Tiny Tim³ as Wang & Ma (2013) did [see equation (4) of Wang & Ma 2013]. Table 7 lists the parameters. The full width at half-maximum (FWHMs) of the adopted PSF in each filter are: 0.067 arcsec for the ACS/WFC *F606W*, 0.071 arcsec for the ACS/WFC *F814W*, 0.069 arcsec for the WFC3/UVIS *F606W* and 0.080 arcsec for the WFC3/UVIS *F814W*.

4.3 Extinction and magnitude transformation

When we fit models to the surface brightness profiles of GC-1 and GC-2, we correct the intensity profiles for extinction. Table 5 lists the effective wavelengths of the ACS/WFC and WFC3/UVIS filters from the Instrument Handbook. With the extinction curve taken from Cardelli, Clayton & Mathis (1989) with $R_V = 3.1$, we derived the A_λ values for each filter. The reddening values of GC-1 and GC-2 having mentioned and used in Section 3 are listed in Table 4.

5 MODEL FITTING

5.1 Structural models

As was done by Barmby et al. (2007), Mclaughlin et al. (2008), Wang & Ma (2013), and Ma (2015), we used three structural models to fit surface profiles of GC-1 and GC-2. These models are developed by King (1966), Wilson (1975) and Sérsic (1968) (hereafter the ‘King model’, ‘Wilson model’ and ‘Sérsic model’, respectively). Mclaughlin et al. (2008) have described the three structural models in detail; here we briefly summarize some of their basic characteristics.

The King model is most commonly used for studies of star clusters, which is the simple model of single-mass, isotropic, modified isothermal sphere. The Wilson model is defined by an alternate modified isothermal sphere based on the ad hoc stellar distribution function of Wilson (1975), which has more extended envelope structures than the standard King isothermal sphere (Mclaughlin et al. 2008). The Sérsic model has an $R^{1/n}$ surface density profile, which is used for parameterizing the surface brightness profiles of early-type galaxies and bulges of spiral galaxies (Baes & Gentile 2011). However, Tanvir et al. (2012) found that some classical GCs in M31 that exhibit cuspy core profiles are well fitted by the Sérsic model of index $n \sim 2 - 6$. The clusters with cuspy cores have usually been called post-core collapse (see Noyola & Gebhardt 2006, and references therein).

³ <http://tinytim.stsci.edu/cgi-bin/tinytimweb.cgi>.

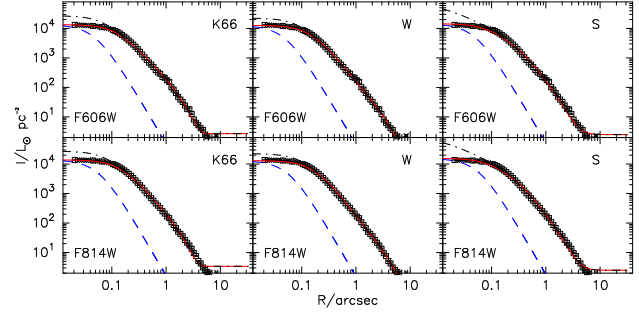


Figure 5. Surface brightness profiles of and model fits to GC-1, with the data of the *F606W* and *F814W* bands from top to bottom. The three panels in each line from left to right are the fits to the King model (K66), Wilson model (W) and Sérsic model (S). The open squares are the data points included in the model fitting, while the crosses are points flagged as ‘DEP’ or ‘BAD’, which are not used to constrain the fit. Dashed (blue) curves trace the PSF intensity profile; bold dash-dotted curves, the unconvolved best-fit model and solid (red) curves, the PSF-convolved best fits.

5.2 Fits

After the intensity profiles were corrected for extinction (see Section 4.3 for details), we fitted models to the brightness profiles of GC-1 and GC-2.

We first convolved the three models with PSFs for the filters used. Given a value for the scale radius r_0 , we computed a dimensionless model profile $\tilde{I}_{\text{mod}} \equiv I_{\text{mod}}/I_0$ and then performed the convolution,

$$\tilde{I}_{\text{mod}}^*(R|r_0) = \iint_{-\infty}^{\infty} \tilde{I}_{\text{mod}}(R'/r_0) \tilde{I}_{\text{PSF}}[(x-x'), (y-y')] dx' dy', \quad (8)$$

where $R^2 = x^2 + y^2$ and $R'^2 = x'^2 + y'^2$. \tilde{I}_{PSF} was approximated using equation 4 of Wang & Ma (2013) (see Mclaughlin et al. 2008, for details). The best-fitting model was derived by calculating and minimizing χ^2 as the sum of squared differences between model intensities and observed intensities with the extinction corrected,

$$\chi^2 = \sum_i \frac{[I_{\text{obs}}(R_i) - I_0 \tilde{I}_{\text{mod}}^*(R_i|r_0) - I_{\text{bkg}}]^2}{\sigma_i^2}, \quad (9)$$

in which a background I_{bkg} was also fitted. The uncertainties of observed intensities listed in Table 6 were used as weights.

We plot the fitting for GC-1 and GC-2 in Figs 5 and 6. The observed intensity profile with extinction corrected is plotted as a function of logarithmic projected radius. The open squares are the data points included in the model fitting, while the crosses are points flagged as ‘DEP’ or ‘BAD’, which are not used to constrain the fit (Wang & Ma 2013). The best-fitting models, including the King model (K66), Wilson model (W) and Sérsic model (S), are shown with a red solid line from the left-hand to the right-hand panel, with a fitted I_{bkg} added. The blue dashed lines represent the shapes of the PSFs for the filters used.

5.3 Main model parameters and derived qualities

Table 8 lists the basic ingredients of all model fits to GC-1 and GC-2, with a simple description of each parameter/column at the end. Error bars on all these parameters (and those on all the derived quantities below) were defined in the same way as in Mclaughlin et al. (2008).

Table 9 contains a number of other structural cluster properties

Table 8. Basic parameters of GC-1 and GC-2 in the M81 group.

ID	Detector	Band	N_{pts}^a	Model	$\chi^2_{\text{min}}^b$	I_{hbg}^c ($L_{\odot} \text{pc}^{-2}$)	W_0^d	c/n^e	μ_0^f (mag arcsec $^{-2}$)	$\log r_0^g$ (arcsec)	$\log r_0^h$ (pc)
(1)	(2)	(3)	(4)	(5)	(6)	(7)	(8)	(9)	(10)	(11)	(12)
GC-1	ACS/WFC	606	40	K66	48.87	2.90 ± 1.20	$8.50^{+0.60}_{-0.57}$	$1.98^{+0.16}_{-0.17}$	$16.11^{+0.25}_{-0.15}$	$-1.450^{+0.015}_{-0.017}$	$-0.205^{+0.015}_{-0.017}$
			40	W	8.84	-0.40 ± 1.15	$7.90^{+0.29}_{-0.27}$	$3.08^{+0.14}_{-0.21}$	$16.03^{+0.07}_{-0.06}$	$-1.350^{+0.011}_{-0.013}$	$-0.105^{+0.011}_{-0.013}$
			40	S	48.78	2.60 ± 0.80	–	$3.10^{+0.08}_{-0.08}$	$16.05^{+0.23}_{-0.17}$	$-3.500^{+0.026}_{-0.046}$	$-2.255^{+0.026}_{-0.046}$
	ACS/WFC	814	38	K66	32.07	4.00 ± 1.98	$8.60^{+0.57}_{-0.51}$	$2.01^{+0.15}_{-0.15}$	$15.45^{+0.17}_{-0.14}$	$-1.500^{+0.051}_{-0.065}$	$-0.255^{+0.051}_{-0.065}$
			38	W	10.90	-1.20 ± 2.55	$7.90^{+0.45}_{-0.36}$	$3.08^{+0.18}_{-0.13}$	$15.43^{+0.08}_{-0.07}$	$-1.350^{+0.014}_{-0.015}$	$-0.105^{+0.014}_{-0.015}$
			38	S	40.30	3.60 ± 1.91	–	$3.05^{+0.11}_{-0.11}$	$17.95^{+0.71}_{-0.67}$	$-3.450^{+0.031}_{-0.035}$	$-2.205^{+0.031}_{-0.035}$
GC-2	WFC3/UVIS	606	46	K66	30.25	2.70 ± 1.02	$8.20^{+0.30}_{-0.28}$	$1.89^{+0.09}_{-0.09}$	$15.83^{+0.10}_{-0.07}$	$-1.100^{+0.015}_{-0.015}$	$0.193^{+0.015}_{-0.015}$
			46	W	10.88	-1.00 ± 0.99	$7.70^{+0.17}_{-0.20}$	$2.95^{+0.11}_{-0.11}$	$15.90^{+0.08}_{-0.08}$	$-1.000^{+0.010}_{-0.008}$	$0.293^{+0.010}_{-0.008}$
			46	S	64.13	2.50 ± 1.33	–	$2.90^{+0.10}_{-0.07}$	$15.74^{+0.15}_{-0.10}$	$-2.950^{+0.028}_{-0.039}$	$-1.657^{+0.028}_{-0.039}$
	WFC3/UVIS	814	46	K66	22.97	3.40 ± 0.90	$7.90^{+0.25}_{-0.27}$	$1.80^{+0.08}_{-0.08}$	$15.22^{+0.08}_{-0.08}$	$-1.050^{+0.018}_{-0.018}$	$0.243^{+0.018}_{-0.018}$
			46	W	4.44	-0.30 ± 0.78	$7.40^{+0.17}_{-0.10}$	$2.69^{+0.14}_{-0.08}$	$15.29^{+0.03}_{-0.02}$	$-0.950^{+0.005}_{-0.008}$	$0.343^{+0.005}_{-0.008}$
			46	S	44.23	2.50 ± 1.23	–	$2.90^{+0.08}_{-0.06}$	$18.15^{+0.92}_{-0.48}$	$-2.950^{+0.030}_{-0.024}$	$-1.657^{+0.030}_{-0.024}$

^a The number of points in the intensity profile that were used for constraining the model fits.

^b The minimum χ^2 obtained in the fits.

^c The best fitted background intensity.

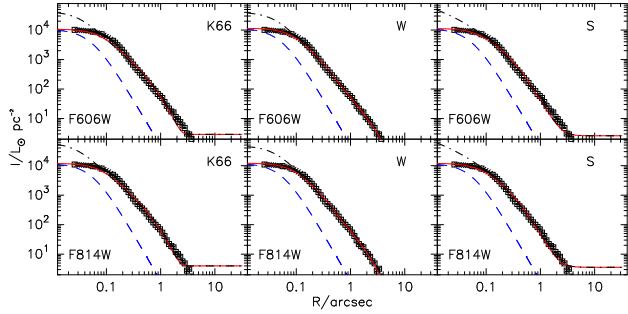
^d The dimensionless central potential of the best-fitting model, defined as $W_0 \equiv -\phi(0)/\sigma_0^2$.

^e The concentration $c \equiv \log(r_t/r_0)$.

^f The best-fitting central surface brightness in the native bandpass of the data.

^g The best model fit scale radius r_0 in arcsec.

^h The best model fit scale radius r_0 in parsec.


Figure 6. Same as Fig. 5, but with surface brightness profiles of and model fits to GC-2.

derived from the basic fit parameters given in Table 8, with a simple description of each parameter/column at the end, and the details of the calculations are presented in Mclaughlin et al. (2008). The uncertainties on all of these derived parameters were estimated in the same way as in Mclaughlin et al. (2008).

Table 10 lists a number of ‘dynamical’ cluster properties derived from the structural parameters already given, plus a mass-to-light ratio (M/L values). As was done by Wang & Ma (2013), the values of the mass-to-light ratios (Υ_V^{pop} in Table 10) in the V band, which were used to derive the ‘dynamical’ parameters, were determined from the population-synthesis models of BC03, assuming a Chabrier (2003) IMF. The ages and metallicities used to compute the Υ_V^{pop} values in the V band are listed in Table 4. The error bars on Υ_V^{pop} include uncertainties in age and $[\text{Fe}/\text{H}]$ listed in Table 4. The uncertainties in these quantities are estimated from their variations around the minimum of χ^2 on the model grids we fit combined in quadrature with the uncertainties in the population-synthesis model Υ_V^{pop} .

We should emphasize that the ‘dynamical’ parameters of GC-1 and GC-2 in Tables 9 and 10 are predicted values and are not directly obtained from spectroscopy measurements. In addition, among the ‘dynamical’ parameters listed in Tables 9 and 10, the predicted line-of-sight velocity dispersions ($\sigma_{p,0}$) can be compared directly to spectroscopic determinations. However, it is unfortunate

that there are not spectroscopic data that can be used to derived measured velocity dispersions of GC-1 and GC-2.

At last, we calculated analogues of the so-called κ parameters of GC-1 and GC-2, and listed them in Table 11. The ‘ κ ’ parameters were introduced by Bender, Burstei & Faber (1992), who define a well-suited orthogonal coordinates in the three-space of the observable parameters. Then, these authors compared the structural properties of ellipticals, bulges, compact ellipticals and dwarf ellipticals (dE) as described in the κ -space, and found that all types of hot stellar systems, except for the very low luminosity dwarf spheroidals, defined planes in this space with possible small, parallel offsets between classes. Mclaughlin et al. (2008) defined the ‘ κ ’ parameters using mass rather than luminosity surface density, as this is more useful for comparing GCs to younger clusters and galaxies. In order to emphasize mass, Mclaughlin et al. (2008) used the notation $\kappa_{m,i}$:

$$\kappa_{m,1} = (\log \sigma_{p,0}^2 + \log R_h) / \sqrt{2} \quad (10)$$

$$\kappa_{m,2} = (\log \sigma_{p,0}^2 + 2 \log \Sigma_h - \log R_h) / \sqrt{6} \quad (11)$$

$$\kappa_{m,3} = (\log \sigma_{p,0}^2 - \log \Sigma_h - \log R_h) / \sqrt{3} \quad (12)$$

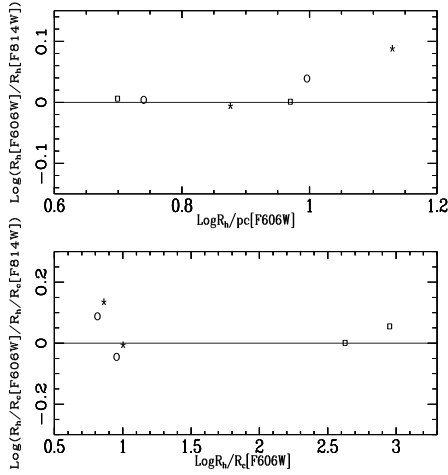
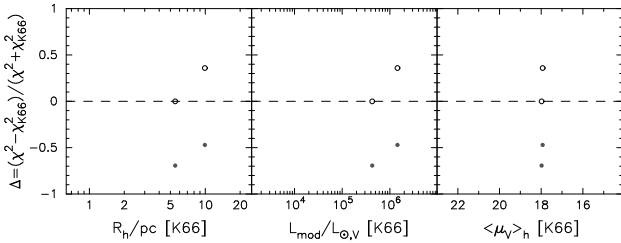
In calculating $\kappa_{m,1}$, $\kappa_{m,2}$, and $\kappa_{m,3}$, the $\sigma_{p,0}$ predicted in Table 10 (Column 11) by adoption of population-synthesis mass-to-light ratios has been used, and Σ_h evaluated by adding $\log \Upsilon_V^{\text{pop}}$ to $\log I_h$ from Column (13) of Table 9. This is evident that $\kappa_{m,3}$ is independent of the assumed mass-to-light ratio. R_h is taken from Table 9 (Column 7) but is in units of kpc rather than pc, for compatibility with the galaxy-oriented definitions of Bender et al. (1992).

5.4 Comparison of fits in the F606W and F814W bands

In this paper, we derived the structural and dynamical parameters from fitting three different models (King 1966, Wilson 1975 and Sérsic 1968) to the radial surface brightness profiles of GC-1 and GC-2 in the F606W and F814W bands. Assessment of the systematic errors and colour dependencies in the fits can be done by com-

Table 11. κ -space parameters of GC-1 and GC-2 in the M81 group.

ID	Detector	Band	Model	$\kappa_{m,1}$	$\kappa_{m,2}$	$\kappa_{m,3}$
(1)	(2)	(3)	(4)	(5)	(6)	(7)
GC-1	ACS/WFC	606	K66	$-0.487^{+0.149}_{-0.161}$	$4.535^{+0.368}_{-0.249}$	$0.112^{+0.095}_{-0.110}$
			W	$-0.305^{+0.122}_{-0.142}$	$4.395^{+0.263}_{-0.297}$	$0.197^{+0.072}_{-0.083}$
			S	$-1.442^{+0.166}_{-0.166}$	$4.096^{+0.266}_{-0.319}$	$-0.677^{+0.086}_{-0.084}$
	ACS/WFC	814	K66	$-0.525^{+0.135}_{-0.159}$	$4.524^{+0.319}_{-0.243}$	$0.080^{+0.084}_{-0.109}$
			W	$-0.301^{+0.184}_{-0.160}$	$4.384^{+0.449}_{-0.354}$	$0.200^{+0.129}_{-0.098}$
			S	$-1.426^{+0.177}_{-0.188}$	$4.120^{+0.243}_{-0.196}$	$-0.663^{+0.095}_{-0.108}$
GC-2	WFC3/UVIS	606	K66	$0.055^{+0.086}_{-0.080}$	$4.654^{+0.167}_{-0.157}$	$0.247^{+0.048}_{-0.038}$
			W	$0.193^{+0.091}_{-0.123}$	$4.476^{+0.179}_{-0.234}$	$0.310^{+0.048}_{-0.053}$
			S	$-0.797^{+0.123}_{-0.136}$	$4.214^{+0.189}_{-0.177}$	$-0.440^{+0.069}_{-0.065}$
	WFC3/UVIS	814	K66	$0.061^{+0.100}_{-0.100}$	$4.754^{+0.240}_{-0.240}$	$0.252^{+0.060}_{-0.060}$
			W	$0.164^{+0.083}_{-0.083}$	$4.676^{+0.133}_{-0.133}$	$0.286^{+0.041}_{-0.041}$
			S	$-0.798^{+0.085}_{-0.134}$	$4.217^{+0.190}_{-0.180}$	$-0.441^{+0.036}_{-0.064}$


Figure 7. Comparison of structural parameters for model fits to the sample clusters observed in both $F606W$ and $F814W$ bands. From top to bottom: projected half-light radius and ratio of half-light to core radius. Open circles: King (1966) model; squares: Sérsic (1968) model; stars: Wilson (1975) model.

Figure 8. Relative quality of fit for Wilson and Sérsic models (filled and open circles) versus King model for the sample clusters in this paper.

band in Fig. 8. Δ is defined as

$$\Delta = (\chi^2_{\text{alternate}} - \chi^2_{\text{K66}}) / (\chi^2_{\text{alternate}} + \chi^2_{\text{K66}}) \quad (13)$$

for comparing the χ^2 of the best fit of an ‘alternate’ model with the χ^2 of the best fit of the King model (see Barmby et al. 2007; Mclaughlin et al. 2008, for details). If the parameter Δ is zero, the two models fit the same cluster equally well. Positive values indicate a better fit of the King model, and negative values indicate the ‘alternate’ model is a better fit than the King model.

The Δ values are plotted as a function of some structural parameters, including the half-light radius R_h , total model lumi-

osity L_{mod} , and the intrinsic average surface brightness $\langle\mu_V\rangle_h$. Fig. 8 shows that GC-1 and GC-2 are significantly better fitted by the Wilson (1975) model than by the King (1966) or Sérsic (1968) models (GC-1 has $\Delta < -0.5$ for the Wilson-model fits and GC-2 has $\Delta \sim -0.5$ for the Wilson-model fits.). In addition, the King (1966) model fits the data of GC-1 and GC-2 somewhat better than the Sérsic (1968) model. These results differ from those for the clusters in NGC 5128 (Mclaughlin et al. 2008), and in M31 (Barmby et al. 2007; Wang & Ma 2013) and M33 (Ma 2015). Mclaughlin et al. (2008) showed that for the clusters in NGC 5128, the Wilson (1975) model fits as well as or better than the King (1966) model; however, Barmby et al. (2007) and Wang & Ma (2013) showed that for most clusters in M31, the King (1966) model fits better than the Wilson (1975) model. Ma (2015) indicated that the King (1966) and Wilson (1975) models fit equally well for nearly all of the M33 sample clusters, and that the Wilson (1975) model fits the M33 sample cluster data better than the Sérsic (1968) model. San Roman et al. (2012) indicated that the M33 young clusters ($\log \text{age} < 8$) are notably better fitted by the Elson-Freeman-Fall model (Elson, Fall & Freeman 1987) with no radial truncation, while the M33 older clusters show no significant differences between the King (1962) and the Elson et al. (1987) fits. In addition, we want to mention that Mclaughlin & van der Marel (2005) showed that globulars and young massive clusters in the Milky Way, Magellanic Clouds and Fornax dSph are systematically better fitted by the Wilson (1975) model than by the King (1966) model, and that the Sérsic (1968) model often fits these globulars and young massive clusters about as well as the Wilson (1975) model but can be significantly worse. GC-1 and GC-2 are most luminous clusters in the local universe. For luminous clusters in M31 and NGC 5128, the results are different. For M31 clusters, Barmby et al. (2007) showed that the bright clusters ($L_{\text{mod}} > 10^5 L_{\odot}$) are better fitted by the King (1966) model; however, for NGC 5128 clusters, Mclaughlin et al. (2008) showed that the bright clusters are generally fitted much better by the Wilson (1975) and Sérsic (1968) models. The results of GC-1 and GC-2 are somewhat different from those of M31 and NGC 5128 clusters. In fact, Barmby et al. (2007) provided the implication that the King (1966) model is more strongly preferred for more luminous M31 clusters. They suggested that the preference for the King (1966) over the Wilson (1975) model is due to some more subtle feature of the observational data that have not yet been isolated. However, the conclusion of Mclaughlin et al. (2008) is that the haloes of GCs in NGC 5128 are generically more extended than the King (1966)

model allows. For GC-1 and GC-2, we consider that they have more extended haloes than the King (1966) model allows.

6 COMPARISON TO PREVIOUS RESULTS AND DISCUSSION

Jang et al. (2012) estimated the ages and masses of GC-1 and GC-2 based on the SDSS *ugriz* data and on the SSP models of BC03. They reported that they derived the ages of GC-1 and GC-2 to be ~ 15.8 Gyr, and the masses to be $\sim 2.51 \times 10^6 M_{\odot}$ for GC-1, and $\sim 7.08 \times 10^6 M_{\odot}$ for GC-2. In this paper, we accurately redetermined the ages and masses of GC-1 and GC-2, based on the improved data and sophisticated fitting methods. In particular, we used the photometric measurements of the 2MASS, which can partially break the age-metallicity degeneracy, in combination with the NVU and optical photometry; and we used the magnitudes in the *UBVRI* and *JHK_s* bands for reducing mass uncertainties resulting from photometric uncertainties based on only the magnitudes in one band. The ages and masses of GC-1 and GC-2 obtained by Jang et al. (2012) and in this paper show that they are old and massive star clusters in the local universe. In particular, their ages show that they are as old as the universe.

Jang et al. (2012) presented the radial surface brightness profiles of GC-1 and GC-2 in the *F814W* band, and they derived the core and half-light radii of GC-1 and GC-2 by fitting the photometric data by the King model and the model of Elson et al. (1987) without considering the PSF. As we know, the apparent core structures of GCs are strongly influenced by the PSF (see Barmby et al. 2007 and McLaughlin et al. 2008 for details). So, it is needed that we redetermined the core radii of GC-1 and GC-2 considering the PSF. In addition, in order to study the properties of GC-1 and GC-2 for details in the future, the other structural and dynamical parameters should be obtained besides the core and half-light radii. So, it is also needed that we derived a wide range of structural and dynamical parameters of GC-1 and GC-2 considering the PSF (see Section 5.2 for details). The structural parameters include the central surface brightness and central potential, concentration indices, core and half-light (effective) radii and total luminosity, and the predicted dynamical parameters include the internal velocity dispersion, total mass, binding energy, central mass density, central escape velocity, relaxation time-scales and phase-space densities. From the King model fits, Jang et al. (2012) derived the core radii of GC-1 and GC-2 to be 0.0755 ± 0.0003 and 0.1269 ± 0.0003 arcsec, respectively. By fitting the King model (King 1966), the core radii of GC-1 and GC-2 obtained here to be 0.0316 ± 0.002 and 0.0891 ± 0.005 arcsec, respectively, based on the radial surface brightness profiles in the *F814W* band. It is seen that the core radii obtained here are smaller than those of Jang et al. (2012). We argue that the difference between the core radii obtained here and those obtained by Jang et al. (2012) resulted from the PSF, i.e. Jang et al. (2012) derived this parameter without considering the PSF. In addition, by fitting the King model (King 1966), the half-light radii obtained here are 5.45 ± 0.22 pc and 9.06 ± 0.21 pc, respectively, based on the radial surface brightness profiles in the *F814W* band, which are in good agreement with those of Jang et al. (2012), who derived the half-light radii of GC-1 and GC-2 to be 6.13 ± 0.01 pc and 9.81 ± 0.01 pc, respectively. However, we should mention that the results of this paper showed that GC-1 and GC-2 are significantly better fitted by Wilson (1975) model than by King (1966) or Sérsic (1968) models. So, we use the half-radii obtained based on the fitting by Wilson (1975) model in Fig. 9.

Some authors derived the masses of the most massive Local Group clusters, such as 037–B327 [$M \sim 8.5 \times 10^6 M_{\odot}$ (Barmby, Holland & Huchra 2002) or $M \sim 3.0 \pm 0.5 \times 10^7 M_{\odot}$ (Ma et al. 2006)] and G1 [$M \sim (7 - 17) \times 10^6 M_{\odot}$ (Meylan et al. 2001) or $M \sim (5.8 - 10.6) \times 10^6 M_{\odot}$ (Ma et al. 2009)] in M31 and ω Cen [$M \sim (2.9 - 5.1) \times 10^6 M_{\odot}$ (Meylan 2002)] in the Milky Way. Martini & Ho (2004) derived the masses of the most luminous GCs in NGC 5128 to range from $M \sim 1.0$ to $M \sim 9.0 \times 10^6 M_{\odot}$. Recently, Mayya et al. (2013) derived the mass of the brightest GC in M81, GC1, to be $M \sim 1.0 \times 10^7 M_{\odot}$. Comparing with these most massive GCs mentioned above, GC-1 and GC-2 are among the most massive clusters in the local universe. In particular, GC-2 is one of the most massive clusters in the local universe. Meylan et al. (2001) argued that the very massive GCs blur the former clear (or simplistic) difference between GCs and dwarf galaxies. In fact, Zinnecker et al. (1988) had proposed that the nucleated dEs would contribute their naked nuclei as a population of GCs when they were accreted and disrupted by a larger galaxy. Martini & Ho (2004) posited that some of the massive GCs in NGC 5128 are nuclei of tidally dwarfs based on their large masses and the possible detection of ‘extratidal light’ by Harris et al. (2002) (but see McLaughlin et al. 2008, for counter-arguments for the massive GCs in NGC 5128). Based on the position of a cluster on the size-luminosity plane, Mackey & van den Bergh (2005) suggested that the most luminous Local Group clusters, such as M54 and ω Centauri in the Milky Way, G1 in M31 and the most luminous clusters in NGC 5128, are the cores of former dwarf galaxies. The large masses of GC-1 and GC-2 may make them different from the rest of the GC population in M81 and M82. Jang et al. (2012) suggested that these two massive clusters are remnants of dwarf galaxies based on the empirically established relation $\log r_h = 0.25 \times M_V + 2.95$ (Mackey & van den Bergh 2005), which forms the upper envelope of Galactic GCs in the M_V versus r_h plane. In Section 5.3, we see that, for both GC-1 and GC-2, the fitted King model (King 1966) falls clearly below the measured profiles at the largest radii, although the model fit was accurate at smaller radii. In fact, Harris et al. (2002) have already found this case for the most luminous GCs in NGC 5128, in which they explained that these clusters exhibit ‘extratidal light’ continuing outward past the nominal tidal radius obtained based on the King (1966) model. These authors further suggested the ‘extratidal light’ as the residual trace of the field-star population of dwarf satellite galaxies, and these most luminous GCs as the luminous compact nuclei of former dwarf satellite galaxies. The large masses and the possible detection of ‘extratidal light’ for GC-1 and GC-2 may present the further evidence that these two GCs are nuclei of tidally dwarfs as suggested by Jang et al. (2012). However, we want to mention the fact that, from Fig. 6, we can see that the Wilson (1975) model can fit the entire profiles of GC-1 and GC-2 accurately without the need to invoke amounts of ‘extratidal light’ implied by the King (1966) model fits. In fact, McLaughlin et al. (2008) argued that the ‘excess’ light implied by the King (1966) model fits to some massive clusters of NGC 5128 is not likely the signature of genuine tidal debris, but a symptom of generic shortcomings in the model itself, i.e. the theoretical basis for it is weak in the low-density and unrelaxed farthest reaches of cluster envelopes, and these authors showed that the Wilson (1975) model can fit these massive clusters of NGC 5128 accurately. The results and comments of McLaughlin et al. (2008) may imply that these massive clusters in NGC 5128 have not the residual trace of the field-star population of dwarf satellite galaxies. So, it is needed to be confirmed in the future that the massive clusters of NGC 5128 are the luminous compact nuclei of former

dwarf satellite galaxies. We argued that GC-1 and GC-2 are in this case. In addition, GC-1 and GC-2 are not the most luminous clusters in M81 and M82 (see Fig. 9). Especially, nearly 20 clusters are more luminous than GC-1. So, we suggested that GC-1 is only a luminous cluster in M81 and M82; however, GC-2 may be different from conventional clusters in M81 and M82. We will discuss GC-2 in detail below. From the Wilson (1975) model fits, the half-light radii of GC-2 obtained here are 13.49 and 11.02 pc based on the radial surface brightness profiles in the $F606W$ and $F814W$ bands, respectively. Its large size and high luminosity ($M_V = -10.63$ mag) makes GC-2 to be an ultra-compact dwarf (UCD) in the M81 group. Fig. 9 shows the half-light radius (R_h) versus absolute magnitude (M_V) diagram, where data for GC-1 and GC-2 are plotted along with those for the GCs (good and spectroscopically confirmed) in M81 (Nantais et al. 2011) and the star clusters (older than 1 Gyr) in M82 (Lim et al. 2013), and for the UCDs from Brodie et al. (2011). In Fig. 9, we used the half-light radii of GC-1 and GC-2 obtained by fitting the radial surface brightness profiles in the $F606W$ band by the Wilson (1975) model. Fig. 9 makes it evident that GC-2 occupies the same area of the UCDs, indicating that GC-2 is a UCD in the M81 group. It is well known that UCDs are compact stellar systems that are more luminous and larger than typical GCs, but more compact than typical dwarf galaxies. They were originally discovered independently by Hilker, Infante & Richtler (1999) and Drinkwater et al. (2000) in spectroscopic surveys of the centre of the Fornax cluster, and they have sizes of $10 < r_h < 100$ pc and luminosities of $M_V < -9$ mag (Liu et al. 2015). Although UCDs have so far been found mostly in dense environments, at the centres of galaxy clusters, or near massive galaxies, they have also been discovered in galaxy groups and even relatively isolated galaxies (see Zhang et al. 2015, for a review). Evstigneeva et al. (2007) discovered one definite and four possible UCD candidates in a photometric search in six galaxy groups. All of these UCDs are intergalactic and not associated with any particular galaxy. Especially, the UCD in the Dorado Group (Evstigneeva et al. 2007) is an intragroup object like GC-2 in the M81 group. As mentioned above, Jang et al. (2012) considered GC-2 to be a remnant of a dwarf galaxy based on the distribution in the M_V versus r_h plane, which accreted to M81 and is receding now. Till now, there has been ongoing debate about the origin of UCDs. A number of different origins of UCDs were brought up: (1) they are merely luminous, genuine GCs (Mieske, Hilker & Infante 2002; Murray 2009); (2) they are the products of the merger of super star clusters (Fellhauer & Kroupa 2002; Bekki et al. 2004); (3) they are the stripped nuclei of dEs (Bekki, Couch & Drinkwater 2001; Bekki et al. 2003; Goerdts et al. 2008); (4) they are remnants of primordial compact galaxies (Drinkwater et al. 2004). Brodie et al. (2011) presented that the M87 UCDs are predominantly stripped nuclei. At the same time, these authors consider it more probable that UCDs have their origins as nuclei that have since been stripped by tidal forces. However, Mieske, Hilker & Infante (2004), Mieske et al. (2006) and Mieske, Hilker & Misgeld (2012) presented that the luminosity and size distribution of UCDs shows a smooth transition to the regime of GCs. So, these authors suggested that, from a statistical point of view, there is no need to invoke an additional formation channel based on the conclusion that the number counts of UCDs are fully consistent with them being the bright tail of the GC population. In addition, Hasegan et al. (2005) and Mieske et al. (2008) presented that, the more massive UCDs show evidence for higher dynamical mass-to-light ratios than those derived from stellar population modelling alone, suggesting that some massive UCDs host a large amount of dark matter

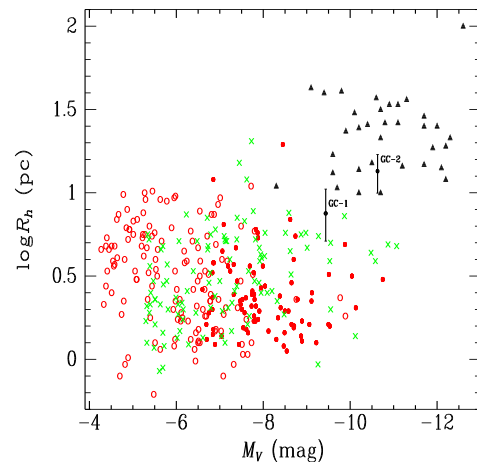


Figure 9. Half-light radii vs. M_V for GC-1 and GC-2 (black dots with error bars) in comparison with GCs (red dots) and GC candidates (red circles) in M81 and star clusters (green crosses) in M82. The black filled triangles are the confirmed ultra-compact dwarfs (UCD) from Brodie et al. (2011).

(see also Pandya, Mulchaey & Greene 2016). For one UCD (M60-UCD1) it has been shown that a massive black hole is responsible for the elevated mass-to-light ratio (Seth et al. 2014). Especially, Mieske et al. (2013) presented two UCD formation channels: one is a ‘globular cluster channel’ which is important mainly for UCDs with $M \lesssim 10^7 M_\odot$ and another is tidal transformation of massive progenitor galaxies which dominates for UCDs with $M \gtrsim 10^7 M_\odot$ and still contributes for lower UCD masses. It is unfortunate that we cannot derive the spectroscopically observed velocity dispersion of GC-2 in this paper, i.e. we cannot derive the dynamical mass of GC-2. In addition, it is true that the mass of GC-2 is smaller than $10^7 M_\odot$. So, we cannot give a clear conclusion of the origin of GC-2 here.

7 SUMMARY

In this paper, we study the two GCs in the remote halo of M81 and M82 in the M81 group: GC-1 and GC-2.

(1) We derive the magnitudes in intermediate-band filters of the BATC system.

(2) We determine these two cluster’s ages and masses by comparing their SEDs (from 2267 to 20000 Å, comprising photometric data in the near-ultraviolet of *GALEX*, 14 BATC intermediate-band and 2MASS near-infrared JHK_s filters) with theoretical stellar population-synthesis models.

(3) The ages of GC-1 and GC-2 obtained in this paper are 15.50 ± 3.20 for GC-1 and 15.10 ± 2.70 Gyr, respectively, which showed that they are old objects in the M81 group.

(4) The masses of GC-1 and GC-2 obtained in this paper are $1.77 - 2.04 \times 10^6$ and $5.20 - 7.11 \times 10^6 M_\odot$, respectively, which showed that they are among most massive clusters in the local universe, especially GC-2 is one of the most massive clusters in the local universe.

(5) We derived the structural and dynamical parameters of GC-1 and GC-2 based on the *HST* images from fitting the surface brightness profiles to three different models combined with the mass-to-light ratios (M/L values) from population-synthesis models.

(6) Catalogues of fundamental structural and dynamical pa-

parameters obtained here are parallel in form to the catalogues produced by McLaughlin & van der Marel (2005) for the GCs and massive young star clusters in the Milky Way, Magellanic Clouds, and the Fornax dwarf spheroidal, by Barmby et al. (2007) and Wang & Ma (2013) for the M31 star clusters, by Ma (2015) for the M33 star clusters, and by McLaughlin et al. (2008) for the NGC 5128 star clusters.

(7) For the first time, we conclude that GC-2 is a UCD in the M81 group based on the r_h versus M_V diagram.

ACKNOWLEDGMENTS

We would like to thank Dr. McLaughlin for his help in finishing this paper. He provide us a table including some parameters which being model-dependent function of W_0 or c . We are indebted to the referee for his/her thoughtful comments and insightful suggestions that improved this paper greatly. This study has been supported by the National Natural Science Foundation of China (NSFC, No. 11373035) and by the National Basic Research Program of China (973 Program, No. 2014CB845702). This study has also been supported by the National Basic Research Program of China (973 Program, Nos. 2014CB845704 and 2013CB834902), by the National Natural Science Foundation of China (NSFC, Nos. 11603035, 11373033, 11433005, 11673027 and 11603034).

REFERENCES

- Baes M., Gentile G., 2011, *A&A*, 525, A136
 Barmby P., Holland S., Huchra J., 2002, *AJ*, 123, 1937
 Barmby P., McLaughlin D. E., Harris W. E., Harris G. L. H., Forbes D. A., 2007, *AJ*, 133, 2764
 Barmby P. et al., 2009, *AJ*, 138, 1667
 Bekki K., Couch W. J., Drinkwater M. J., 2001, *ApJ*, 552, L105
 Bekki K., Couch W. J., Drinkwater M. J., Shioya Y., 2003, *MNRAS*, 344, 399
 Bekki K., Couch W. J., Drinkwater M. J., Shioya Y., 2004, *ApJ*, 610, L13
 Bender R., Burstein D., Faber S. M., 1992, *ApJ*, 399, 462
 Brodie J. P., Romanowsky A. J., Strader J., Forbes D. A., 2011, *AJ*, 142, 199
 Bruzual A. G., Charlot, S., 2003, *MNRAS*, 344, 1000 (BC03)
 Cardelli J. A., Clayton G. C., Mathis J. S., 1989, *ApJ*, 345, 245
 Chabrier G., 2003, *PASP*, 115, 763
 Chandar R., Ford H. C., Tsvetanov Z., 2001, *AJ*, 122, 1330
 Chiboucas K., Jacobs B. A., Tully R. B., Karachentsev I. D., 2013, *AJ*, 146, 126
 Drinkwater M. J., Gregg M. D., Phillipps S., 2000, *PASA*, 17, 227
 Drinkwater M. J., Gregg M. D., Couch W. J., Ferguson H. C., Hilker M., Jones J. B., Karick A., Phillipps S., 2004, *PASA*, 21, 375
 Elson R. A. W., Fall S. M., Freeman K. C., 1987, *ApJ*, 323, 54
 Evstigneeva E. A., Drinkwater M. J., Jurek R., Firth P., Jones J. B., Gregg M. D., Phillipps S., 2007, *MNRAS*, 378, 1036
 Fan X. et al., 1996, *AJ*, 112, 628
 Fellhauer M., Kroupa P., 2002, *MNRAS*, 330, 642
 Goerdt T., Moore B., Kazantzidis S., Kaufmann T., Macció A. V., Stadel J., 2008, *MNRAS*, 385, 2136
 Harris W. E., Harris G. L. H., Holland S. T., McLaughlin D. E., 2002, *AJ*, 124, 1435
 Hasegan M. et al., 2005, *ApJ*, 627, 203
 Hilker M., Infante L., Richtler T., 1999, *A&AS*, 138, 55
 Jang I. S., Lim S., Park H. S., Lee M. G., 2012, *ApJ*, 751, L19
 Jenkner H., Lasker B. M., Sturch C. R., McLean B. J., Shara M. M., Russel J. L., 1990, *AJ*, 99, 2082
 King I. R., 1962, *AJ*, 67, 471
 King I. R., 1966, *AJ*, 71, 64
 Lim S., Hwang N., Lee M. G., 2013, *ApJ*, 766, 20
 Liu C. Z. et al., 2015, *ApJ*, 812, L2
 Ma J., 2015, *AJ*, 149, 157
 Ma J., de Grijs R., Yang Y., Zhou X., Chen J., Jiang Z., Wu Z., Wu J., 2006, *MNRAS*, 368, 1443
 Ma J. et al., 2009, *Res. Astron. Astrophys.*, 9, 641
 Ma J. et al., 2010, *PASP*, 122, 1164
 Ma J. et al., 2012, *AJ*, 143, 29
 Ma J. et al., 2013, *Res. Astron. Astrophys.*, 13, 339
 Mackey A., van den Bergh S., 2005, *MNRAS*, 360, 631
 Martini P., Ho L. C., 2004, *ApJ*, 610, 233
 Mayya Y., Rosa-González D., Santiago-Cortés M., Rodríguez-Merino L. H., Vega O., Torres-Papaqui J. P., Bressan A., Carrasco L., 2013, *MNRAS*, 436, 2763
 McLaughlin D. E., van der Marel R. P., 2005, *ApJS*, 161, 304
 McLaughlin D. E., Barmby P., Harris W. E., Forbes D. A., Harris G. L. H., 2008, *MNRAS*, 384, 563
 Meylan G., 2002, in Geisler D., Grevel E. K., Minniti D., eds, *ASP Conf. Ser. Vol. 207, IAUS, Extragalactic Star Clusters*. Astron. Soc. Pac., San Francisco, p. 555
 Meylan G., Sarajedini A., Jablonka P., Djorgovski S., Bridges T., Rich R., 2001, *AJ*, 122, 830
 Mieske S., Hilker M., Infante L., 2002, *A&A*, 383, 823
 Mieske S., Hilker M., Infante L., 2004, *A&A*, 418, 445
 Mieske S., Hilker M., Infante L., Jordán A., 2006, *AJ*, 131, 2442
 Mieske S. et al., 2008, *A&A*, 487, 921
 Mieske S., Hilker M., Misgeld I., 2012, *A&A*, 537, 3
 Mieske S., Frank M. J., Baumgardt H., Lützgendorf N., Neumayer N., Hilker M., 2013, *A&A*, 558, A14
 Monachesi A. et al., 2013, *ApJ*, 766, 106
 Morrissey P. et al., 2007, *ApJS*, 173, 682
 Murray N., 2009, *ApJ*, 691, 946
 Nantais J. B., Huchra J. P., Zeza A., Gazeas K., Strader J., 2011, *AJ*, 142, 183
 Noyola E., Gebhardt K., 2006, *AJ*, 132, 447
 Oke J. B., Gunn J. E., 1983, *ApJ*, 266, 713
 Pandya V., Mulchaey J., Greene J. E., 2016, *ApJ*, 819, 162
 Puzia T. H., Zepf S. E., Kissler-Patig M., Hilker M., Minniti D., Goudfrooij P., 2002, *A&A*, 391, 453
 Rey S. C. et al., 2007, *ApJS*, 173, 643
 Rhodes J. D., Massey R., Albert J., Taylor J. E. Koekemoer A. M., Leauthaud A., 2006, in Koekemoer A. M., Goudfrooij P., Dressel L. L., eds, *The 2005 HST Calibration Workshop: Hubble After the Transition to Two-Gyro Mode*, NASA, Greenbelt, p. 21
 Rich R. M., Shara M. M., Zurek D., 2001, *AJ*, 122, 842
 Salpeter E. E., 1955, *ApJ*, 121, 161
 San Roman I., Sarajedini A., Holtzman J. A., Garnett D. R., 2012, *MNRAS*, 426, 2427
 Schlegel D. J., Finkbeiner D. P., Davis M., 1998, *ApJ*, 500, 525
 Sérsic J. L., 1968, *Atlas de Galaxias Australes*. Obs. Astronomico, Cordoba
 Seth A. C. et al., 2014, *Nature*, 513, 398
 Stetson P. B., 1987, *PASP*, 99, 191
 Tanvir N. R. et al., 2012, *MNRAS*, 422, 162
 Wang S., Ma J., 2012, *AJ*, 143, 132
 Wang S., Ma J., 2013, *AJ*, 146, 20

- White R. E., Shawl S. J., 1987, *ApJ*, 317, 246
Wilson C. P., 1975, *AJ*, 80, 175
Yan H. J. et al., 2000, *PASP*, 112, 691
Zhang H. X. et al., 2015, *ApJ*, 802, 30
Zheng Z. Y. et al., 1999, *AJ*, 117, 2757
Zhou X. et al., 2003, *A&A*, 397, 361
Zhou X. et al., 2004, *AJ*, 127, 3642
Zinnecker H., Keable C. J., Dunlop J. S., Cannon R. D., Griffiths W. K., 1988, *Proc. IAU Symp. 126, The Harlow-Shapley Symposium on Globular Cluster Systems in Galaxies*. Kluwer, Dordrecht, p. 603